JOURNAL OF SPACECRAFT AND ROCKETS
Vol. 33, No. 1, January–February 1996

Three-Dimensional Computational Analysis of Complex Launch Vehicle Configurations

Grant Palmer* and Pieter Buning†
NASA Ames Research Center, Moffett Field, California 94035
Herb Yanowitz‡
EER Systems Corporation, Seabrook, Maryland 20706
and
Ethiraj Venkatapathy§
Thermosciences Institute, Moffett Field, California 94035

Computational fluid dynamic analysis is performed on the Conestoga 1620 vehicle configuration at Mach 0.8 and 1.49 points along its ascent trajectory. Because the vehicle geometry is complex, flow solutions were obtained using a technique where overlapping volume grids are generated over each individual component. Calculations were performed to evaluate the pressure loading on the structural components, compute aerodynamic drag, and determine the effect the pressure distribution would have, if any, on booster separation. Pressure loading on the wire tunnels was found to exceed original design limits, and the wire tunnels were strengthened as a result of this study. There was no evidence of flow impingement on the motor nozzles. Pressure forces on the strap-on boosters do not appear as though they will hinder booster separation.

Nomenclature

c_p = specific heat, lbm/ft^3
p = pressure, lb/in.^{2}
R = gas constant, 1716 ft^2/(s^2 − R)
Re = Reynolds number, $\rho ul/\mu$
u = velocity, ft/s
y = initial grid spacing, ft
μ = viscosity, (lb − s/ft^2)
ρ = density, lbm/ft^3

Introduction

THE Conestoga space launch vehicle, developed by EER Systems Corporation, is designed to launch U.S. Government, commercial, and international payloads ranging from 500 to 5000 lb into low Earth orbit.[1] With modifications, the vehicle can also meet the special requirements for geosynchronous orbit and planetary missions.

The Conestoga launch vehicle consists of from two to six solid rocket motor strap-on boosters surrounding a core motor. The strap-on boosters are nominally Thiokol Corporation Castor IVA and/or Castor IVB solid rocket motors, whereas the core motor is generally a Castor IVB. Thiokol XL's and Hercules GEM motors may also be used. The core motor may contain one or two upper stage motors and are usually solid rockets, but other designs exist. The payload is contained in an aerodynamic fairing (6-ft nominal diameter) situated on top of the core motor. Total vehicle length ranges from 50 to 70 ft with gross weights of approximately 85,000–255,000 lb.

Computational fluid dynamic (CFD) analysis was performed around the Conestoga 1620 first-stage configuration. The purpose of this paper is to perform detailed calculations to provide the following information about the vehicle.

1) Determine whether the pressure loads on the wire tunnels connecting the core motor and strap-ons, the interface module (IFM), and the fairing exceed design limits.

2) Compute pressure loads on the Castor IVB motor vectoring nozzles. The vectoring nozzles are used to trim the vehicle if it is subject to buffeting on ascent. If there is significant flow impingement on the nozzles, the pressure loads may prevent proper rotation of the nozzle.

3) Calculate vehicle drag at several Mach numbers and compare against experimental data.

4) Provide vehicle pressure distribution for control analysis.

5) Compute separation pressures on the first-stage strap-on boosters. If the pressure is higher on the side facing away from the core motor than on the side facing the core motor, booster separation may be impeded.

Flow solutions were performed at points along the ascent trajectory corresponding to freestream Mach numbers of 0.8 and 1.49. These conditions were chosen because they were at the lower and upper bounds of the transonic regime and because wind-tunnel data existed at these Mach numbers.

Vehicle Description

The Conestoga 1620 configuration for a proposed mission consists of four Castor IVB and two Castor IVA strap-on boosters. The Castor IVB strap-on motors have vectoring nozzles protected by shrouds. The core thrust ring located at the rear of the core booster motor case contains thrust bearings and attach points for the aft strap-on jettison thrusters. The core stabilizer ring contains the attachment points for the forward structural connections between the core motor and strap-on boosters. These structural connections are also referred to as the wire tunnels. The wire tunnels contain electronic wiring, ordnance lines, and the forward strap-on jettison thrusters. The IFM attaches at its lower end to the core stabilizer ring and at its upper end to the fairing.

Two Castor IVA and two Castor IVB strap-on motors are ignited at liftoff and carry the vehicle through maximum dynamic pressure at approximately 45 s into the flight. The first stage Castor IVA and Castor IVB motors are jettisoned after burnout at 54.5 and 63 s, respectively. The two second-stage Castor IVB motors are ignited at 59 s, burn out at 123 s, and are jettisoned 3 s later. The core Castor IVB motor is ignited at 119 s and burns to 184 s. The Castor IVB

Presented as Paper 94-1863 at the AIAA 12th Applied Aerodynamics Conference, Colorado Springs, CO, June 20–22, 1994; received Sept. 27, 1994; revision received July 5, 1995; accepted for publication Aug. 23, 1995.

*Research Scientist, Reacting Flow Environments Branch, Mail Stop 230-2. Senior Member AIAA.
†Research Scientist, Applied Aerodynamics Branch. Senior Member AIAA.
‡Aerospace Engineer.
§Research Scientist. Member AIAA.

motor burnout is followed by payload fairing jettisoning, upper stage separation from the core motor, coast to apogee, and ignition of the upper stage motor. The total time from liftoff to orbital insertion is 546 s. This is a typical trajectory for the 1620 configuraiton. The actual trajectory may vary according to payload mass, desired orbit, and type of solid rocket engines used.

Solution Methodology

Grid Generation

The Conestoga 1620 vehicle with its strap-on booster rockets and connecting hardware is a complex configuration that would be extremely cumbersome to represent using a single grid. A multiple grid scheme is used to solve for the flow around this vehicle. Each individual component is modeled with a single grid that overlaps its neighbor grids. Information is passed back and forth across the overlap boundaries using interpolation stencils. Figure 1a shows the surface geometry of the launch vehicle that was provided by EER. Because of bilateral symmetry, only one-half of the vehicle was considered in the flow computations. In subsequent discussions, the first-stage Castor IVA and IVB motors will be referred to as 1A1 and 1B1, respectively. The second stage Castor IVB motors are designated 2B1 and 2B2.

Figure 1b shows a close-up view of the region near the core thrust ring with the 1A1 and 1B1 motors removed from view. The surface grids representing the spherical thrust bearings and the aft strap-on jettison thrusters overlap the core and strap-on booster motor grids. Collar grids were used to provide a suitable overlap between the thrust bearing and strap-on booster grids. Figure 1c shows a similar close-up of the region near the core stabilizer ring.

The Conestoga vehicle geometry was modeled using 28 volume grids including core motor, strap-on booster, wire tunnel, jettison thruster, thrust bearing, thrust bearing collar, and surrounding box grids. The thrust bearing collar grids provide a suitable overlap between the thrust bearing and strap-on booster grids. The total number of grid points was 2.8×10^6. Volume grids were generated using the hyperbolic grid generator HYPGEN.[2] HYPGEN creates the volume grid by marching away from the surface grid. The marching direction and stretching function are determined by user inputs and from solving orthogonality relations and a cell volume constraint equation. The initial grid spacing, calculated from the Reynolds number and estimated skin friction coefficient, was set to 5.0×10^{-5}. This corresponds to setting the nondimensionalized grid spacing, $y^+ = \rho u^* y/\mu = 1$.

A formal grid sensitivity study was not performed. The primary objective of the computations was to obtain surface pressure on the vehicle components. Pressure is less sensitive to grid resolution than other quantities, such as heat transfer, and it was felt that maintaining an initial nondimensional grid spacing, $y^+ = 1$, was sufficient to accurately resolve the surface pressure.

The computer code PEGSUS[3] was used to determine interpolation stencils for each grid with respect to adjacent grids and to ensure that volume grids did not penetrate solid boundaries. The resulting grid and interpolation data files are used by the flow solver. The quality parameter that specifies the tolerances for the interpolation stencils was set to range from 0.9 to 0.8. Of the 35,166 boundary points in the 28 volume grids, there were 532 orphan points, where PEGSUS was unable to find an interpolation stencil within the specified quality tolerances. This amounts to 1.5% of the boundary points.

Solution Algorithm

Flow solutions about the Conestoga launch vehicle were generated with the OVERFLOW code.[4] This code is a general-purpose Reynolds-averaged Navier–Stokes flow solver, with a variety of boundary conditions and physical modeling options. The OVERFLOW code evolved from the F3D code[5] and was developed in part for simulating the flow about the Space Shuttle launch vehicle.[4] As in F3D, OVERFLOW uses the Chimera overset grid approach for handling complex geometries.

Several numerical algorithms are available as options in the OVERFLOW code. Convective fluxes can be modeled using central differencing plus Jameson type second- and fourth-order artificial dissipation or Roe upwinding. Implicit algorithms include Beam–Warming[6] approximate factorization and a diagonalized approximate factorization of Pulliam and Chaussee.[7] Two turbulence modeling options are available in OVERFLOW, the Baldwin–Lomax algebraic model and the Baldwin–Barth one-equation model.[8]

For computation over the Conestoga vehicle, the three-factor diagonal implicit solution algorithm was used. The diagonalized scheme is preferable for steady-state problems due to a reduced operation count. Inviscid fluxes were centrally differenced with

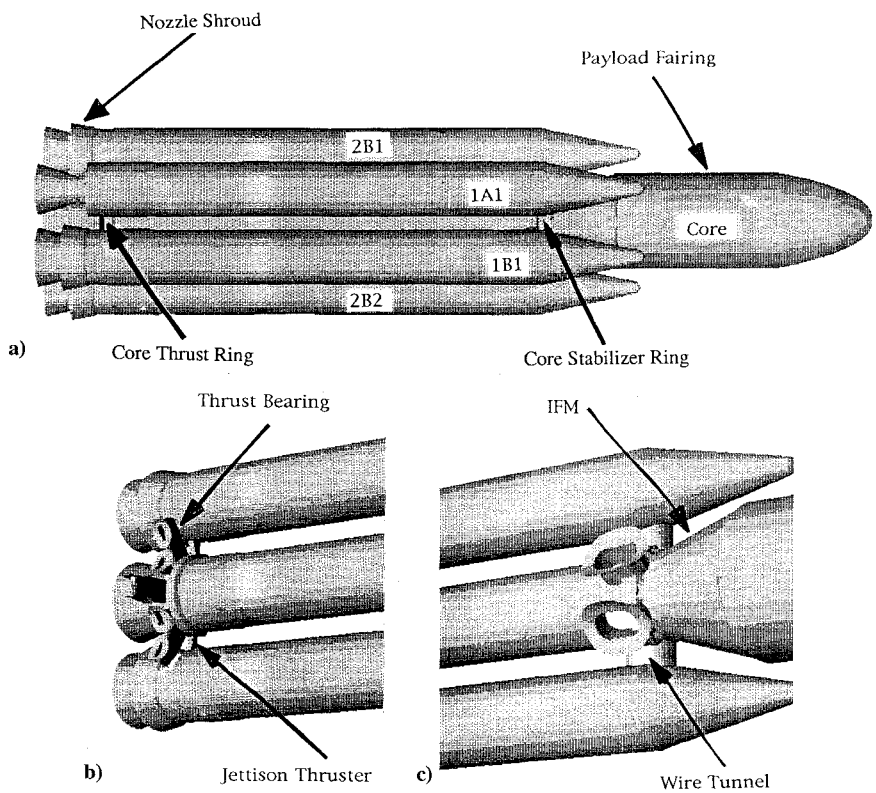

Fig. 1 Vehicle geometry: a) first-stage configuration, b) close-up of core thrust ring region, and c) close-up of core stabilizer ring region.

Table 1 Freestream conditions

Mach	h, ft	v, ft/s	T, °R	P, psi	Re/ft
0.8	8,253	1765	489.3	10.8	$4.525e+6$
1.49	20,540	2437	445.5	6.6	$5.792e+6$

second- and fourth-order dissipation applied to both the explicit and implicit terms. Viscous fluxes were modeled using the thin-layer approximation. The Baldwin–Barth model was chosen for this study because of its ability to handle the complex geometry and overset grids.[9]

Initial and Boundary Conditions

Freestream conditions for the Mach 0.8 and 1.49 trajectory points are presented in Table 1 and correspond to 24 and 36 s into the flight. No-slip, adiabatic wall-boundary conditions were used on the motors and connecting hardware surfaces. Zero-pressure gradient was enforced normal to the wall. Symmetry, freestream, and axis boundary conditions were employed where appropriate.

Results

Comparison with Experimental Pressure and Drag

Tests were conducted on a 1/20th-scale Conestoga 1620 model in the LTV Aerospace and Defense Company high-speed wind tunnel.[10] Both first- and second-stage configurations were tested. The models were sting mounted in the test facility. Pressure transducers were flush mounted along the top of the core motor from the nose to the bottom of the IFM and at various locations on one of the second-stage motors. Force and moment coefficients were calculated from data obtained from a sting-mounted, six-component balance. Tests were conducted at Mach numbers ranging from 0.3 to 4.75 and at Reynolds numbers ranging from 4 to 12 $\times$ 10^6/ft.

One difference between the experimental model and the computational vehicle configuration is that due to structural considerations the wire tunnels were made larger after the completion of the wind-tunnel tests. The computational configuration incorporated the larger wire tunnels; the experimental model did not. The computational data should predict higher pressure in front of the wire tunnels than that shown by experimental measurements. Also, the experimental model was mounted on a sting whereas the computation model was not. The Mach 0.8 wind-tunnel test was performed at a Reynolds number of 5.3 $\times$ 10^6/ft as compared to the Mach 0.8 flight condition value used in the CFD computation of 4.525 $\times$ 10^6/ft. At Mach 1.49, the wind-tunnel and CFD Reynolds numbers were 7.0 $\times$ 10^6/ft and 5.792 $\times$ 10^6/ft, respectively.

Figure 2a compares computed and experimental pressure values along the core motor at Mach 0.8 from the nose to the aft end of the IFM. Pressure drops from its stagnation point value as the flow expands around the nose and gradually rises along the length of the fairing due to the influence of the strap-on boosters and wire tunnels. There is a second expansion at the fairing/IFM interface. Pressure then rises due to blockage caused by the wire tunnel and core stabilizer ring. The experimental and computational data agree reasonably well except at the nose-fairing interface where the experimental data show a stronger expansion than predicted by the computation. A possible reason for this is inadequate longitudinal grid resolution in the expansion region. The effect of the larger wire tunnel can be seen in that computed pressure along the IFM increases more rapidly and reaches a higher peak value than that seen experimentally.

Figure 2b shows experimental and computed pressure values at Mach 0.8 along the length of the 2B1 motor on the side away from the core motor. As the flow travels along the length of the motor, expansions occur after the spherical nose and at the interface between the conical and cylindrical sections. The pressure spike near the aft end of the conical section is due to a slope discontinuity in the cone geometry. Pressure gradually increases along the cylindrical body. A sharp spike occurs when the flow hits the nozzle shroud and there is a flow expansion off the back end of the shroud. Pressure increases along the length of the nozzle but remains below the freestream pressure indicating no significant flow impingement on the nozzle. Only three experimental data points are available for comparison. No experimental data were available

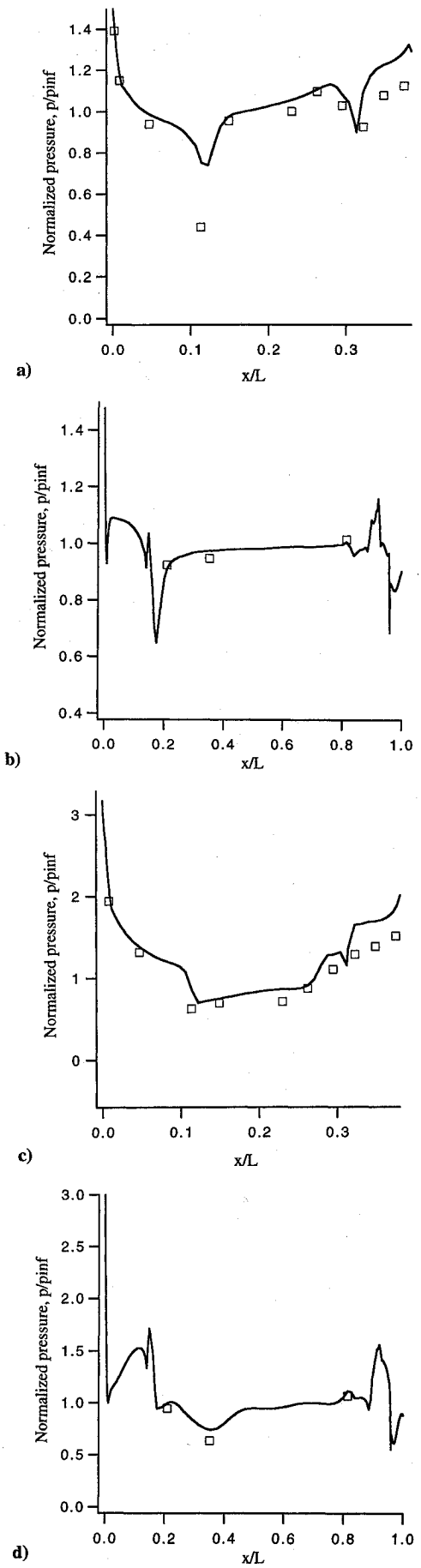

Fig. 2 Experimental and computational surface pressure comparison: a) core motor, M = 0.8; b) 2B1 motor, M = 0.8; c) core motor, M = 1.49; and d) 2B1 motor surface pressure, M = 1.49. ——, Computation; □, experiment.

Table 2 Component percentage contribution to overall vehicle drag

Component	$M = 0.8$	$M = 1.49$
Core motor	8.6	10.8
A motors	16.3	19.5
B motors	28.9	38.7
Wire tunnels	32.6	19.4
Thrust bearings	10.7	8.5
Jettison thrusters	1.9	1.7
Collar grids	1.0	1.4

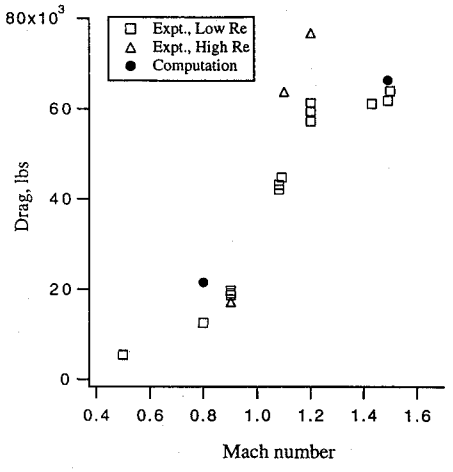

Fig. 3 Computed and experimental drag.

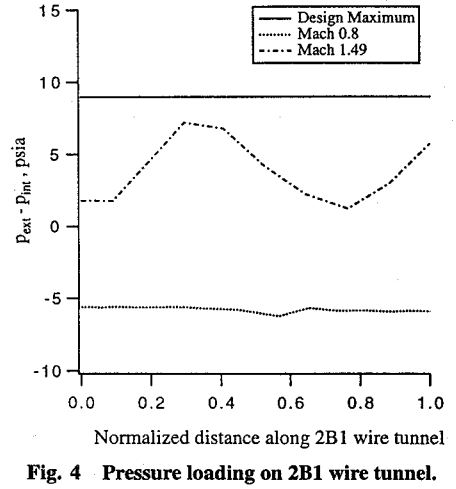

Fig. 4 Pressure loading on 2B1 wire tunnel.

in the nose, shroud, or nozzle region. Experimental pressure measurements taken along the cylindrical portion of the motor compare reasonably well with the computed values.

Calculated and experimental data over the core motor for the Mach 1.49 case are compared in Fig. 2c. The pressure profile shows similar characteristics to the Mach 0.8 solution except the region of high pressure in front of the wire tunnels is more extensive, extending almost the entire length of the IFM. The Mach 1.49 computation did a better job of predicting the expansion at the nose-fairing interface, which was weaker than that seen with the Mach 0.8 case. Agreement between the experimental and computational pressure values is generally good. Once again, the computed surface pressure is higher in the region in front of the wire tunnel, probably due to the geometrical differences between the two configurations. Figure 2d shows Mach 1.49 pressure data over the 2B1 motor and is similar to that seen at Mach 0.8.

Figure 3 presents computed and experimental vehicle drag results. Two sets of experimental data were taken; one set at lower Reynolds number per foot values ranging from 3.8 to 7.0 $\times$ 10^6/ft and another set at higher Reynolds number values ranging from 8.1

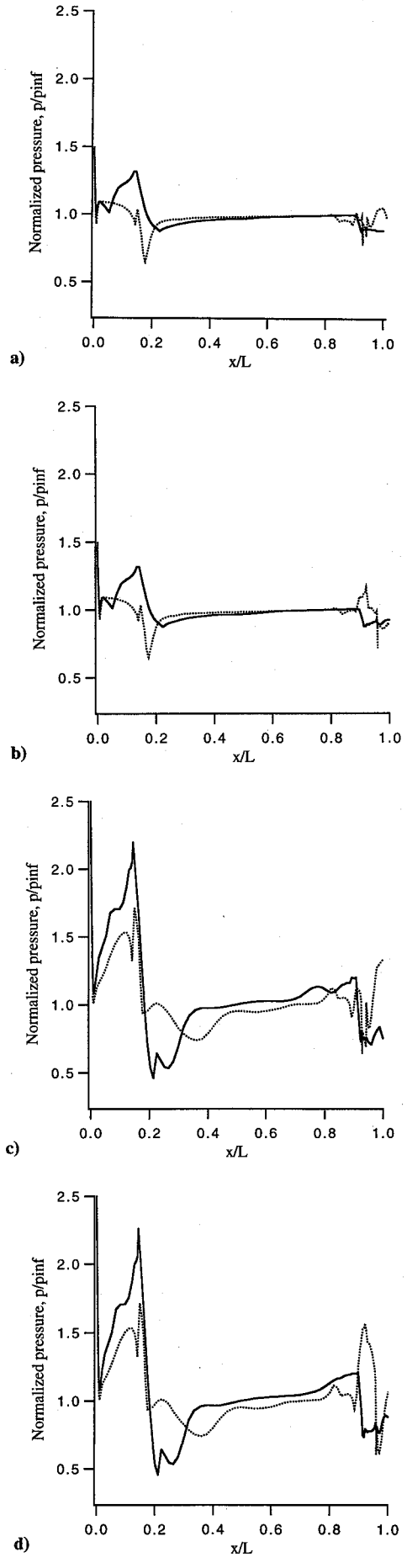

Fig. 5 Separation pressures, 1A1 and 1B1 boosters: a) 1A1 booster, Mach 0.8; b) 1B1 booster, Mach 0.8; c) 1A1 booster, Mach 1.49; and d) 1B1 booster, Mach 1.49. ——, Inside face; - - - -, outside face.

to 8.7×10^6/ft. The computations were for Reynolds number per foot values of 4.2 and 5.8×10^6/ft, corresponding to the middle of the lower range. The experimentally obtained drag coefficient data was corrected to the zero base drag condition,[10] matching the assumption made in the numerical computations. The Mach 1.49 computed drag value agrees very closely with the experimental date and is easily within the range of measurement uncertainty. The Mach 0.8 computational drag is higher than the experimental values. This is in part a consequence of the underprediction of the strength of the expansion around the core nose, as seen in Fig. 2a. Also, the increased thickness of the wire tunnel in the computational vehicle geometry would result in a higher drag prediction.

Table 2 breaks the overall computational vehicle drag into the percentages contributed by each component. The wire tunnels, though relatively small in size, make a significant contribution to overall vehicle drag, particularly in the transonic case. The wire tunnels experience significant pressure loading.

Pressure Loading on Structural Components

Pressure profiles were examined on the wire tunnels to determine if the pressure loading exceeded design limits. The wire tunnels have some internal pressure and were designed to withstand a maximum pressure differential of 9 psi. Figure 4 shows the pressure differential, $p_{ext} - p_{int}$, on the leading edge of the 2B1 wire tunnel. The wire tunnels are initially sealed, and the internal pressure assumed to be the sea level value of 14.7 psi. The Mach 0.8 external pressure is below this value and is within design limits. The maximum pressure differential in the Mach 1.49 case is 7.3. If there is leakage in the wire tunnel seal, the internal pressure may drop as the vehicle ascends and the Mach 0.8 and 1.49 pressure differentials would increase. Even the 7.3 value is close to the design limit representing a potential failure mode of the vehicle and, as a result of this study, the wire tunnels were strengthened.

The 1A1 and 1B1 strap-on boosters separate from the core motor at 54.5 and 63 s into the flight, respectively. To achieve proper separation, the surface pressure on the side facing away from the core motor should not be significantly higher than that on the inside face. Figure 5 shows pressure profiles along the line intersecting the wire tunnel and aft jettison thruster and on along outside of the booster 180 deg from the first line for the 1A1 and 1B1 boosters at Mach 0.8 and 1.49. These conditions correspond to flight times of 24 and 36 s, respectively. In all four cases there is a net outward force that pushes the booster away from the core at separation, as well as a moment that will tend to push the nose of the boosters away from the core motor.

Conclusions

CFD analysis was successfully performed on the Conestoga 1620 vehicle configuration at the Mach 0.8 and 1.49 points along its ascent trajectory. The flow solution was obtained using a Chimera technique, where overlapping volume grids are generated over each individual component. Computed pressure profiles and vehicle drag compared reasonably well with experimental data. A high-pressure region due to blockage caused by the wire tunnels and core stabilizer ring extended upstream from the wire tunnels along the entire length of the IFM. There is no evidence of significant flow impingement on the B motor nozzles. The wire tunnels, though relatively small in size, made a significant contribution to overall vehicle drag. Pressure loading on the wire tunnels was found to exceed original design limits, and the wire tunnels were strengthened as a result of this study. Pressure forces on the 1A1 and 1B1 boosters do not appear as though they will hinder booster separation.

Acknowledgment

Support for E. Venkatapathy provided through a contract from NASA (NAS2-14031) to Eloret is gratefully acknowledged.

References

[1]Daniels, M., and Saavedra, B., "The Conestoga Launch Vehicle—A Modular Approach to Meeting User Requirements," AIAA Paper 94-0893, Feb. 1994.

[2]Chan, W. M., Chiu, I. T., and Buning, P. G., "User's Manual for the HYPGEN Hyberbolic Grid Generator and the HGUI Graphical User Interface," NASA TM 108791, Oct. 1993.

[3]Suhs, N. E., and Tramel, R. W., "Pegsus 4.0 User's Manual," Arnold Engineering Development Center, AEDC-TR-91-8, Arnolds AFB, TN, June 1991.

[4]Buning, P. G., Chiu, I. T., Obayashi, S., Rizk, Y. M., and Steger, J. L., "Numerical Simulation of the Integrated Space Shuttle Vehicle in Ascent," AIAA Paper 88-4359, Aug. 1988.

[5]Ying, S. X., "Three-Dimensional Implicit Approximately Factored Schemes for the Equations of Gasdynamics," Ph.D. Thesis, Dept. of Aeronautics and Astronautics, Stanford Univ., Stanford, CA, June 1986.

[6]Beam, R. M., and Warming, R. F., "An Implicit Factored Scheme for the Compressible Navier–Stokes Equations," *AIAA Journal*, Vol. 16, No. 4, 1978, pp. 393–402.

[7]Pulliam, T. H., and Chaussee, D. S., "A Diagonal Form of an Implicit Approximate Factorization Algorithm," *Journal of Computational Physics*, Vol. 39, No. 2, 1981, pp. 347–363.

[8]Baldwin, B. S., and Barth, T. J., "A One-Equation Turbulence Transport Model for High Reynolds Number Wall-Bounded Flows," NASA TM 102847, Aug. 1990.

[9]Renze, K. J., Buning, P. G., and Rajagopalan, R. G., "A Comparative Study of Turbulence Models for Overset Grids," AIAA Paper 92-0437, Jan. 1992.

[10]Felber, M. L., "A Transonic and Supersonic Wind Tunnel Test on a 0.05 Scale Conestoga Launch Vehicle Over the Mach Range of 0.30 to 4.8," LTV Aerospace and Defense Co., HSWT Test 1142, Dallas, TX, May 1992.

K. J. Weilmuenster
Associate Editor